Layer-dependent properties and non-collinear spin structure of epitaxial antiferromagnetic Mn films on Co/Cu(001)

Jiaming Song ,[1] Chii-Bin Wu,[1, 2] Bin Zhang,[1] Jianli Xu,[3] Wolfgang Kuch[1]

1. *Freie Universität Berlin, Institut für Experimentalphysik, Arnimallee 14, 14195 Berlin, Germany*

2. *Chung Yuan Christian University, Department of Physics, Chungli 32023 Taiwan, R. O. C.*

3. *Fudan University, State Key Laboratory of Surface Physics, 200433 Shanghai, P. R. China*

Email: kuch@physik.fu-berlin.de

Abstract

The surface of expanded face-centered tetragonal (e-fct) antiferromagnetic Mn films of a few atomic monolayers thickness grown epitaxially on Co/Cu(001) was investigated at room-temperature by scanning tunneling microscopy and scanning tunneling spectroscopy using a ferromagnetic ring-shaped bulk iron probe. We show that the main contribution to the contrast modulation observed as a function of Mn thickness in differential conductance maps is not due to spin-polarized tunneling from a layer-wise antiferromagnetic spin alignment. Instead, it is mainly of electronic origin resulting from layer-dependent electronic properties of the Mn film, probably related to different levels of intermixing with Co atoms. On the atomic scale, the Mn surface demonstrates a geometrical reconstruction with a (12×2) periodicity in two orthogonal domains on the four-fold symmetric substrate with an apparent surface corrugation of up to 0.3 Å. Simultaneously recorded differential conductance maps show different textures in the two orthogonal domains, providing evidence for non-collinearity in the Mn surface spin structure.

Introduction

The antiferromagnetic (AFM) spin structure in low-dimensional systems has been drawing significant attention in the past decade.[1–7] Not until the magnetic exchange anisotropy was discovered[8], ferromagnetic/antiferromagnetic (FM/AFM) coupled systems are being harnessed because of the unique magnetic behaviors of AFM layers. In nature, there are two kinds of single element AFM crystals, Chromium (Cr) and Manganese (Mn). Since Mn displays diverse phases on different crystalline lattices under different conditions[9–14], the magnetic properties of ultra-thin films of this single-element metal epitaxially grown on FM substrates have been attracting more and more researchers to explore. Due to the strained and distorted lattice of the e-fct structure, Mn with this crystalline structure is metastable, nonetheless, it can be both structurally and magnetically stabilized when epitaxially grown on, for example, fct Co/Cu(001).[15] In order to interpret the Mn AFM spin configurations in AFM/FM exchange-coupled systems, e-fct Mn/Co(001) became an AFM/FM model system because both metals are single elements and the pseudomorphic growth facilitates achieving a well-defined interface. According to an ab-initio study of e-fct Mn, a (001)-plane-confined $c(2\times2)$ compensated collinear spin structure is predicted.[16] For ultra-thin AFM films, because of the vanishing net magnetic moment, many fundamental magnetic properties are not easily probed directly. A magneto-optical Kerr effect (MOKE) experiment showed no oscillation of the saturation Kerr ellipticity as a function of the Mn thickness in Mn/Co/Cu(001).[15] The enlarged coercivity after Mn deposition further supported an in-plane compensated AFM spin configuration at the interface.[15] However, there is still no direct proof for the two-dimensional (2D) collinear compensated spin structures. On the surface of low-dimensional Mn films, because of the broken inversion symmetry, unique magnetic spin structures might be found different from the bulk. Spin-polarized scanning tunneling microscopy (Sp-STM)[17,18] facilitates exploring the surface Mn spin configuration in real space and provides a distinct tool to view the Mn surface even on the atomic scale[14,19–21]. Recent Sp-STM studies,

including our own, of AFM fct Mn on Co/Cu(001) at both low[22] and room temperatures[23] have imaged Mn surfaces on relatively large scales and indeed observed a layer-wise contrast difference between successive Mn layers. The observed layer-wise contrast of the Mn surface suggests an in-plane layer-wise uncompensated AFM spin configuration and fits to the prediction of the AFM/FM exchange-coupled system with a collinear in-plane spin structure. However, the lateral resolution achieved in all previous studies did not allow conclusions on the atomic-scale Mn spin configuration, which still remains unknown.

Here we show that the previously observed scanning tunneling spectroscopy (STS) contrast in constant-current images of the surface of Mn/Co/Cu(001) is not strictly alternating when increasing the Mn layer thickness in steps of single atomic layers, as would be expected for a magnetic origin, and, furthermore, does not reverse for opposite magnetization direction of the Co layer. It has thus to be of mainly non-magnetic origin, related to different electronic properties at different local Mn thicknesses. Auger electron spectroscopy (AES) shows that Co atoms from the underlying Co films are being incorporated into the Mn film. We suggest that the variation of the level of intermixing with Co atoms as a function of Mn thickness is the main reason for the layer-wise spectroscopic contrast observed previously in this system, possibly coexisting with a minor contribution from a layered AFM spin configuration. .

A more detailed look into the surface of the Mn films by high-resolution Sp-STM at room temperature, using a bulk iron ring as spin-polarized scanning probe[23], reveals a (12×2) geometric reconstruction of the Mn surface as well as evidence for a non-collinear Mn surface spin structure of the same periodicity. We attribute this atomic-scale non-collinear spin structure, which differs from the predicted 2D spin structures with collinear $c(2\times2)$ compensated[15,16] and in-plane uncompensated[22,23] AFM configurations to the presence of competing exchange interactions in the frustrated and reconstructed Mn film.

Experiment

The experiment was performed in an ultra-high vacuum chamber with a base pressure of 1×10^{-10} mbar. A disk-shaped Cu(001) single crystal with a diameter of 10 mm was used as substrate. It was cleaned by cycles of Ar^+ sputtering with ion energy of 1 keV and subsequent annealing to 900 K for 30 min. The smoothness and cleanliness of the crystal surface was examined by low-energy electron diffraction (LEED), AES, and scanning tunneling microscopy (STM) to make sure that a defect-free surface is achieved. Molecular beam epitaxy was used for the thin film deposition. Co and Mn were evaporated while the sample was held at room temperature. Co was evaporated from a Co rod with a purity of 99.95%, which was bombarded with electrons, while Mn was evaporated by electron bombardment of Mn pieces with 99.95% purity in a molybdenum crucible. During Co evaporation, medium-energy electron diffraction (MEED) was employed to monitor the evaporation rate from the intensity oscillations of the specular beam intensity. Co exhibits a coherent layer-by-layer growth mode on Cu(001) at room temperature[24,25], which facilitates thickness calibration from MEED oscillations during Co evaporation. Afterwards AES and STM were used for the more accurate Co thickness determination. The Mn thickness was calibrated by AES and STM. No trace of oxygen could be observed in AES within the detection limit of about 2%, neither before nor after the STM measurements. To explore the magnetic properties of the sample, *in-situ* longitudinal MOKE measurements were performed. A room temperature STM (Omicron 1) was used for the STM measurements. A lock-in amplifier [modulation voltage and frequency: 20 mV, 2.38 kHz] facilitates extracting the second-harmonic term of the signal and the differential conductance map can be obtained simultaneously with the constant-current topography during the scanning process. The scanning probe is a ferromagnetic Fe ring-shaped probe with an in-plane magnetic sensitivity[23], fitting to the expected in-plane magnetization direction of the system.[15,16]
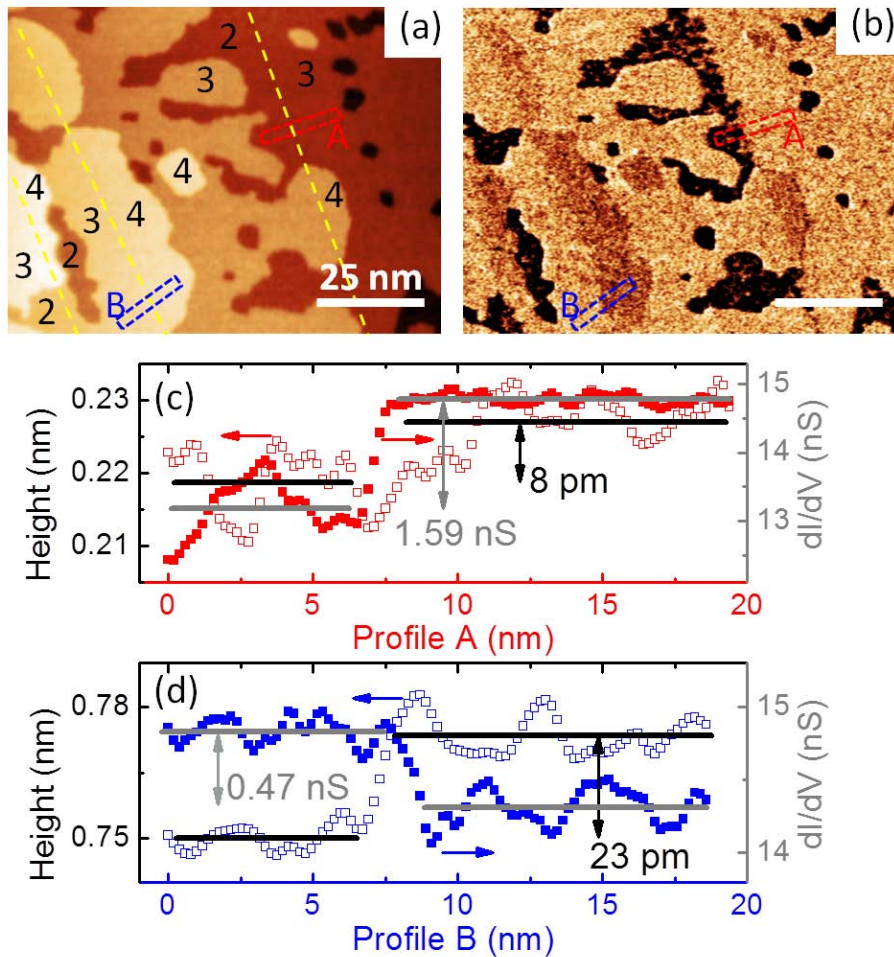
Results

FIG. 1. (Color online) Constant current topography (a) and simultaneously recorded dI/dV map (b) at sample bias +0.15 V, tunneling current 2.8 nA. Yellow dashed lines in (a) indicate overgrown Co steps underneath the Mn layer. Red and blue dashed rectangles labeled "A" and "B" indicate the positions where line profiles have been taken. (c), (d) Plots of line profiles of A and B, taken from left to right while averaging pixels across the width of the rectangles. Open and solid scattered symbols are for topography and dI/dV signal from (a) and (b), respectively.

At room temperature, Mn exhibits a step-flow layer-by-layer growth mode above 1 ML thickness on the fct Co/Cu(001) surface. FIG. 1 (a) shows the topography of 3 ML Mn/4 ML Co/Cu(001) with three layers Mn (2nd, 3rd, 4th) exposed, as indicated by numbers in some places. Yellow dashed lines schematically mark the overgrown Co step edges. FIG. 1 (b) is

the corresponding differential conductance map recorded at the same time. In this *dI/dV* map, the Mn surface exhibits a clear three-level layer-wise contrast with a very dark–bright–dark sequence on 2nd, 3rd, 4th layers. On the same Mn terrace across the Co step edge underneath, the contrast reverses with one monolayer more overgrown Mn on the next Co step. FIG. 1 (c) and (d) present line profiles A and B taken from both the topography image and the differential conductance map at the positions indicated in (a) and (b). In the topography, on the same Mn terrace, both regions A and B show a larger height where Mn has overgrown a Co step edge because of the larger Mn vertical lattice constant compared to that of Co.[22,26] However, the step heights between 2 and 3 ML Mn (profile A) and 3 and 4 ML Mn (profile B) appear different. The step between 3 and 4 layers is more than two times higher than that between 2 and 3. Though both values are close to the vertical interlayer distance difference between fct Mn and Co and the slight deviation from the literature value[22,26] could be due to the accuracy of the *z* piezo calibration, the 15 pm height difference between steps in profiles A and B still cannot be explained by assuming the same electronic property of different layers. From the profiles of the differential conductance map we also learn that the contrast difference between 2 and 3 ML is about 3.4 times that between 3 and 4 ML. Considering that a magnetic STM probe is used, the extracted *dI/dV* signal cannot be interpreted alone by an in-plane layer-wise uncompensated AFM spin configuration of Mn.[22,23]
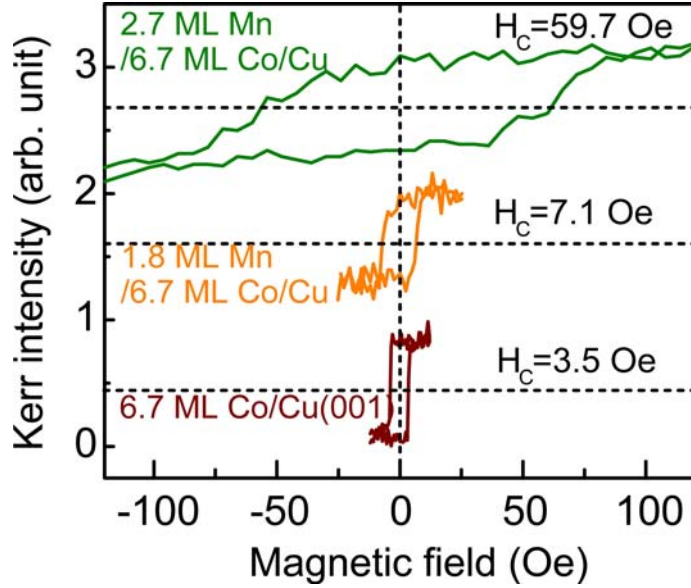
FIG. 2. (Color online) Longitudinal MOKE hysteresis loops for 6.7 ML Co/Cu(001) (bottom), 1.8 ML Mn/6.7 ML Co/Cu(001) (middle), and 2.7 ML Mn/6.7 ML Co/Cu(001) (top).

In order to confirm that the thickness range for Mn with the observed layer-wise contrast is above the critical thickness of Mn for AFM order at room temperature, we performed *in-situ* longitudinal MOKE measurements. The magnetic field was applied along the [110] in-plane easy axis of Co. FIG. 2 shows hysteresis loops of 6.7 ML Co/Cu(001) without and with 1.8 ML and 2.7 ML Mn on top. Bare Co has a small coercivity of 3.5 Oe. When 1.8 ML Mn is deposited, the coercivity is slightly increased to 7.1 Oe. However, after deposition of 2.7 ML Mn, a pronounced enlargement of coercivity appears and the value reaches about 60 Oe, indicating AFM behavior of Mn at this thickness. The critical thickness for Mn on this 6.7 ML Co template should thus be between 1.8 ML and 2.7 ML which is, at room temperature, close to Kohlhepp's result[27]. Although the interfacial Co roughness influences the Mn critical thickness, the critical thickness deviation between filled and half-filled Co layers is less than 1 ML[28], such that the Mn thicknesses discussed in this paper should be above the critical thickness.
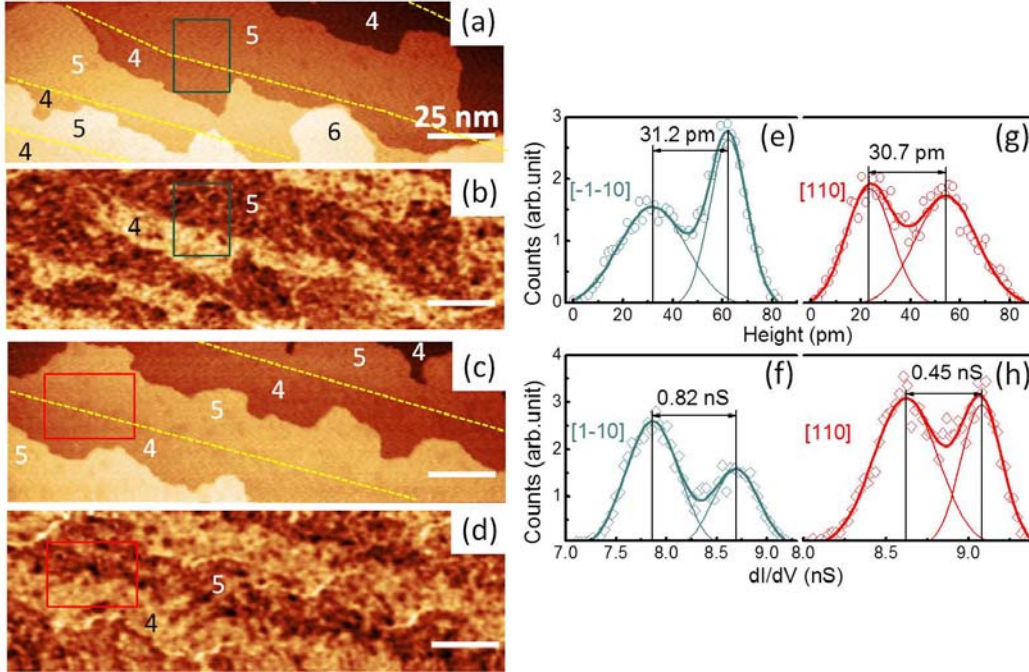
FIG. 3. (Color online) (a) (c) STM topography images of Mn on 5 ML Co/Cu(001) with 4th and 5th Mn layers exposed. Before Mn deposition, Co layers were magnetized along [-1-10] and [110] directions for (a) and (c), respectively. (b) (d) Simultaneously recorded *dI/dV* maps of (a) and (c). Yellow dashed lines indicate overgrown Co steps underneath. Feedback parameters: +0.2 V, 2.0 nA. (e), (f), (g), (h) are histograms for areas within the rectangles in (a), (b), (c), (d), respectively.

According to the assumption of a layer-wise uncompensated AFM spin model for Mn[22,23], where the spin direction of the first Mn ML is pinned to the Co magnetization direction[29,30], an oppositely magnetized Co layer should give rise to opposite spin contrast for the same thickness of AFM Mn on top when measured with the same probe. FIG. 3 (a) and (c) show topographic surfaces of the same thickness of Mn with oppositely magnetized FM Co underneath. The height difference between the 4th and the 5th ML Mn across the overgrown Co step on the same Mn terrace is almost the same, as shown by histograms in FIG. 3 (e) and (g). Nevertheless, in the *dI/dV* maps in FIG. 3 (b) and (d) corresponding to the two Co magnetization directions, always the 5th layer appears darker than the 4th layer. This rules out that the observed *dI/dV* contrast is simply due to spin-polarized tunneling from Mn surface

layers with layer-wise uncompensated spin structure. The histograms of the *dI/dV* map exhibit different contrast levels, as shown in (f) and (h). The variation of Mn differential conductance between the 4th and 5th ML Mn on top of the Co layer magnetized along the [110] direction [FIG. 3 (f)] turns out to be about half of that on top of the Co layer magnetized along the [-1-10] direction. In FIG. 3 (a) and (b), there is also a small patch of 6th ML Mn visible. Here it is seen that the *dI/dV* contrast between 5th and 6th ML Mn is much smaller than the one between 4th and 5th, similar to the observation from FIG. 1 about 2nd, 3rd, and 4th Mn layer [to be discussed later].
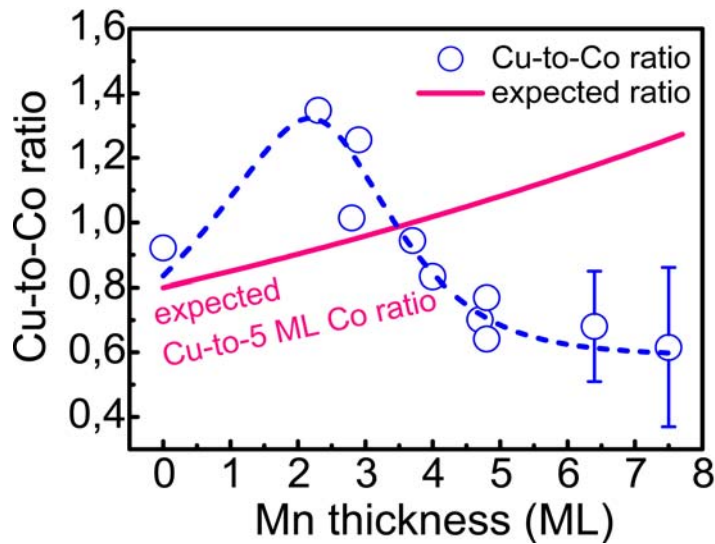

FIG. 4. (Color online) Cu-to-Co ratio of Auger electron intensity of Mn/5 ML Co/Cu(001) as a function of Mn thickness. Cu and Co peaks in the spectra at electron energies of 920 eV and 716 eV, respectively, were used. Open circles represent experimental Cu-to-Co ratios, the solid curve shows the trend expected from the inelastic mean free paths of Cu and Co Auger electrons, the dashed curve is a guide to the eye. Error bars increase at higher Mn overlayer thicknesses as indicated, due to low signal.

Since the spin contrast of an in-plane layered uncompensated AFM spin structure alone cannot explain the observed layer-wise *dI/dV* contrast of the Mn surface, we have to conclude that there must be also a layer-dependent non-magnetic electronic contribution to the differential conductance maps. A possible explanation for that comes from AES data: FIG. 4

shows the Cu-to-Co ratio of AES intensities of Mn/Co/Cu(001) as a function of Mn thicknesses for different sample preparations where the Co thickness was always 5.0±0.2 ML. The data points marked by open circles represent the experimental Cu-to-Co peak ratios. Since the Cu Auger electrons have a longer inelastic mean free path due to their higher kinetic energy (920 eV) compared to Co Auger electrons (716 eV), the Cu signal is less attenuated by overlayers, and the Cu-to-Co peak ratio is supposed to increase with increasing Mn overlayer thickness. The experimental data, on the contrary, are seen to decrease in the Mn thickness regime between 2 and 6 ML. Assuming inelastic mean free path lengths of 5.45 and 4.1 ML for Cu and Co, respectively[31], an increase like shown by the solid line in FIG. 4 would be expected. The deviation from this behavior could be a hint towards a certain amount of Co segregation into the initial capping Mn atomic layers during room-temperature deposition. Accordingly, there should be less segregated Co atoms at the surface of thicker Mn layers, which could explain the layer-dependent variation of the electronic properties reflected in the *dI/dV* maps. Nonetheless, we cannot exclude that also a layer-wise component of the AFM spin structure is present, which could be the reason for the different *dI/dV* contrast between 4 and 5 ML Mn for opposite Co magnetization in FIG. 3 (f) and (h).
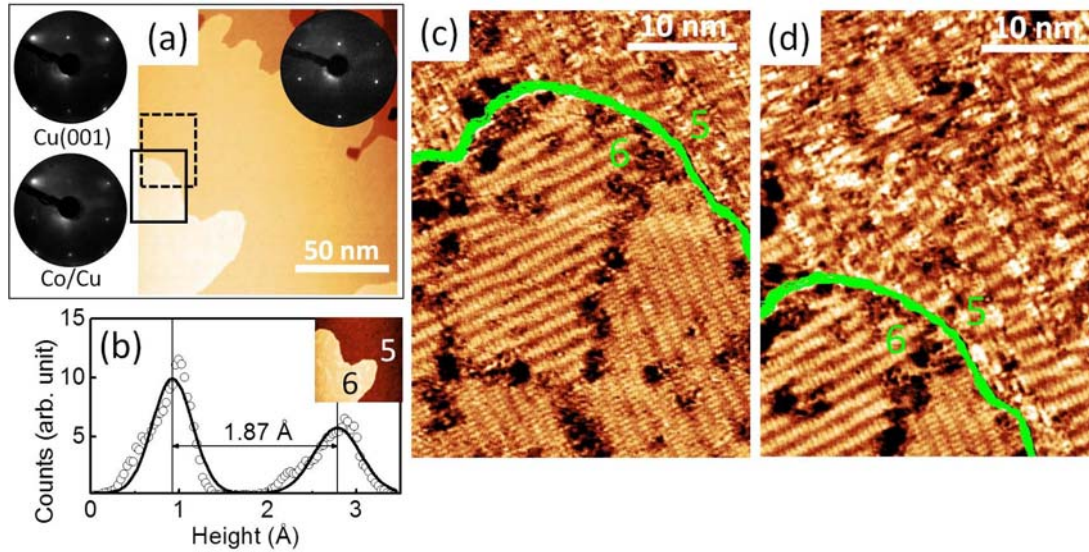
FIG. 5. (Color online) (a) Constant current topography of the Mn surface (sample bias +0.2 V, tunneling current 2.5 nA). The inset shows the LEED pattern of the same Mn surface at 117.8 eV electron energy. The LEED pictures on the left show patterns obtained for Cu(001) (top) and 4 ML Co/Cu(001) (bottom) at the same energy. (b) Histogram of a part of the topography image cropped from (a), as shown in the inset. (c), (d) Constant-current dI/dV maps corresponding to areas marked by solid and dashed rectangles in (a), respectively (sample bias +0.2 V, tunneling current 10.5 nA). Green boundaries highlight the step edges between regions of 5 (top) and 6 ML Mn thickness (bottom).

In order to investigate the AFM spin configuration of the e-fct Mn surface on the atomic scale, we performed high-resolution STM and STS measurements on a 5.4 ML Mn film on 4.0 ML Co/Cu(001). The step height between two adjacent Mn layers amounts to 1.87 Å according to the histogram presented in FIG. 5 (b). This step height is consistent with the vertical interlayer distance of the e-fct Mn film on Co/Cu(001)[22,26]. The LEED pattern of this film is shown in the right inset of FIG. 5 (a). Compared to the sharp $p(1\times1)$ spots on both clean Cu(001) and 4 ML Co/Cu(001), the Mn LEED image is also dominated by sharp $p(1\times1)$ spots at the same positions as those of the Co substrate, but the background intensity is somewhat enhanced. This suggests a dominating pseudomorphic growth of Mn on the fcc Co(001) template. However, indications for a surface reconstruction of Mn/Co/Cu(001) have been observed before.[26] They have been interpreted as being confined to the surface and not reflecting the

major bulk structure.

FIG. 5 (c) and (d) are differential conductance maps of the areas marked by solid and dashed rectangles in FIG. 5 (a), showing the exposed 6 ML and 5 ML Mn terraces, respectively. On both terraces, there exist two types of domains with stripes oriented in two mutually orthogonal directions. On the 6 ML terrace, as best seen in FIG. 5 (c), these stripes form larger ordered domains compared to the 5 ML terrace in (d). Similar domains with the same stripe features were also observed in other areas with Mn thicknesses of 5 ML and 6 ML. The 6 ML areas always contain longer-range-ordered stripes, whereas the 5 ML areas only possess some smaller striped domains mixed together with disordered areas.
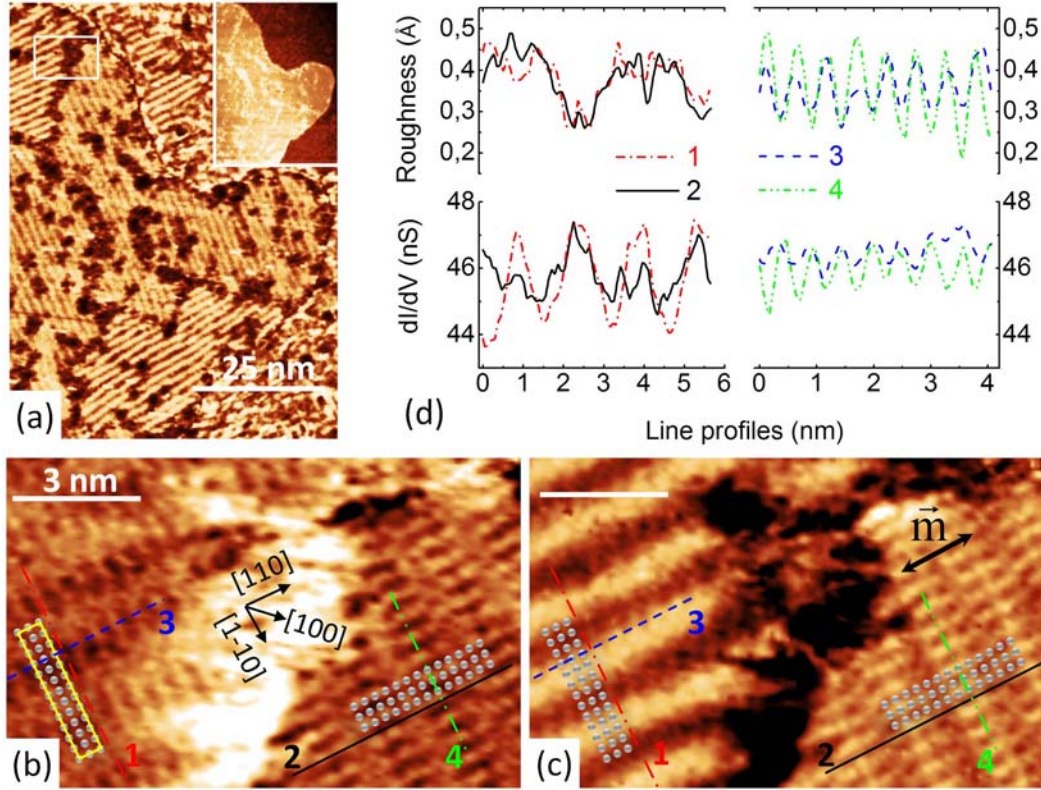
FIG. 6. (Color online) (a) Constant current *dI/dV* map at 6 ML Mn thickness (sample bias +0.2 V, tunneling current 10.5 nA). The inset shows the corresponding simultaneously recorded topography image. (b), (c) High-resolution topography and *dI/dV* map of the area marked by a white rectangle in (a) (sample bias +0.2 V, tunneling current 10.5 nA). The black double-sided arrow in (c) shows the Fe ring orientation, the yellow rectangle in (b) indicates the unit cell of the (12×2) superstructure, and small gray balls indicate Mn surface atoms. (d) Line profiles taken from (b) and (c). Line profiles 1, 2, 3 and 4 correspond to lines marked by respective line styles in (b) and (c). The line profiles from (b) are taken exactly at the same sample positions as those from (c).

FIG. 6 (a) is a differential conductance map from a larger area of 6 ML Mn thickness with long-range-ordered stripe domains. The inset shows the corresponding topography image recorded during the same scan. In order to acquire more detailed information about the two orthogonally-oriented stripes, high-resolution scanning was performed on a typical area as marked by the white rectangle in FIG. 6 (a). The high-resolution topography image and differential conductance map are shown in FIG. 6 (b) and (c), respectively. In (b), a

corrugated surface with two orthogonal domains in the left and the right part of the image is observed. Both show the same periodicity, as demonstrated by taking and comparing line profiles 1 and 2 for one direction, 3 and 4 for another direction. The corresponding profiles are illustrated in FIG. 6 (d). Line profiles of the topography illustrate that the apparent surface corrugation amounts up to about 0.3 Å. According to the periodicity measured from profiles 1 and 3 (or 2 and 4), a (12×2) superstructure unit cell can be identified on the surface, as highlighted by the yellow rectangle in FIG. 6 (b). The white circles represent the position of Mn atoms within one unit cell.

While the topography of the two domains is virtually the same, just rotated by 90°, the differential conductance contrast shows notable differences. The left domain exhibits a different periodicity, as evidenced by the line profiles in FIG. 6 (d). Line profile 1 (left area) in the *dI/dV* map has half the periodicity of line profile 2 (right area), and also half of the topographic periodicity of line profile 1. Moreover, in FIG. 6 (c), the amplitude of profile 2 is not identical to the one of profile 1, but about 20% less. We interpret these notable differences to originate from spin contrast influence, where the orientation of the tip magnetization breaks the symmetry present in the topography image. The orientation of the iron ring probe is illustrated by the black arrow in the differential conductance map in FIG. 6 (c). The magnetic moment of the apex atom is along the tangential direction of the ring. Since this magnetic moment has a larger component along the [110] direction, the contribution from spin contrast should be dominated by the spin component of Mn atoms along this direction.

The strong similarity of the (12×2) superstructure in the two 90°-rotated domains in the constant-current topography image [FIG. 6 (b)] means that it is mainly of non-magnetic origin. It is plausible to assume that there is a corresponding geometric reconstruction of the Mn film. Vertically expanded pseudomorphic films often exhibit a geometric reconstruction and/or surface buckling.[12,32–34] This opens the question why no (12×2) superstructure is observed in the LEED image shown in the inset of FIG. 5 (a), just an enhanced background. A possible

explanation could be that over the whole sample, the fraction of large ordered stripe domains could be relatively small compared to the fraction of short-range-ordered and disordered domains, in particular in regions of 5 ML thickness. A further complication could be the small size of structurally well-ordered domains that exhibit the (12×2) superstructure. Although the regions imaged in FIG. 5 and FIG. 6 consist of domains somewhat larger than the transfer width of the LEED system (typically 10 nm), this might not be the case in many other regions of the sample. In regions with 5 ML Mn thickness, particularly small ordered patches, possibly even with locally slightly different periodicities, for example at their edges, coexist with disordered regions and regions of less order.

Discussion

In order to interpret the atomic-scale contrast difference between the two orthogonally-orientated domains in the differential conductance maps of FIG. 6, we extract possible models for the spin structure of the reconstructed Mn surface. We first smooth the experimental data for one unit cell of the right and left domain of FIG. 6 (c) on the lengthscale of atomic distances, average over a few unit cells, and set a zero line such that the average dI/dV contrast is zero. The resulting contrast maps are shown in FIG. 7 (b) and (c), which then represent the average experimental dI/dV signal for an x- and y-aligned tip, respectively. The red double-sided arrows indicate the directions of spin sensitivity. As in the experiment [see line profiles 1 and 2 in the bottom of FIG. 6 (d)], the maximum amplitude of the spin polarization projected on the x direction [FIG. 7 (b)] is about 20% lower than in the y projection [FIG. 7 (c)]. Before proceeding further, we have to consider that in addition to a spin-polarized contribution to the dI/dV signal, there might be also a non-spin-polarized one, arising from the geometric (12×2) reconstruction. This non-magnetic contribution should be independent of the tip orientation. We approximate this non-magnetic contribution by the experimental contrast of the constant-current topography image. The topography signal from the right-hand side of FIG. 6 (b) was smoothed in the same way as described above.

Depending on the weighting factor that describes the weight of the non-magnetic contribution, different spin structures can be extracted from the experimental data. We take the contrast of FIG. 7 (b) and (c), reduced by the non-magnetic contrast, as proportional to the x and y component of the atomic spins, as it is usually assumed in spin-polarized tunneling[17,35]. Hereby the decay of the spin polarization into the vacuum is assumed to be equal for both spin directions. To extract also the absolute value of the z component, we assume that the absolute values of all atomic spins are equal and assign zero z component to the largest in-plane spin. Setting now the non-magnetic contribution to zero, i.e., assuming spin-polarized tunneling as the sole source of the observed dI/dV contrast, leads to the spin structure shown in FIG. 7 (a). It shows an area in the xy plane with a size of 61.5 Å×18.7 Å. In this simulated map, the yellow rectangle marks the (12×2) unit cell, and black circles represent sites of Mn atoms. A non-collinear spin structure is obtained, as presented by arrows, which show the projection of the atomic spin moments on the xy plane. The color bar on the right indicates the absolute value of the z component of the spins. In this spin structure, the averaged in-plane spin moment within one unit cell is zero, i.e., all spins compensate in the xy plane if summed up. The sign of the z component is undetermined. One could assume a checkerboard-like arrangement of the sign of the z component in order to have the relative orientation of the spins of neighboring atoms closer to 180°.
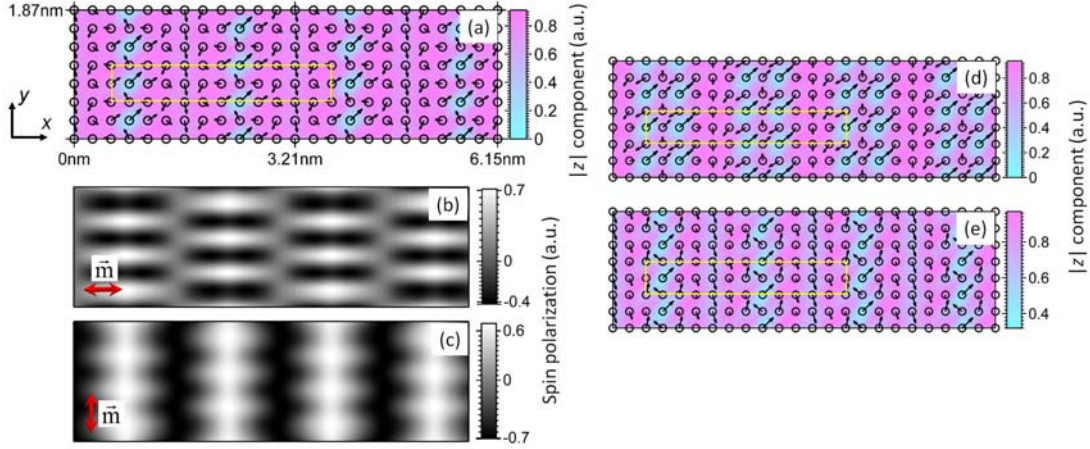
FIG. 7. (Color online) (a) Simulated non-collinear spin structure of the reconstructed Mn surface, assuming only spin contrast in the *dI/dV* maps. Black arrows show the orientation and absolute values of each atomic spin projected in the *xy* plane and the color bar on the right represents the absolute magnitude of the *z* components of spins (see text). Black circles represent Mn atomic sites. (b), (c) Smoothed and periodically extended experimental *dI/dV* maps obtained from the right and left parts of FIG. 2 (c) (see text). Red arrows show the ring orientations. (d), (e) Two other possible non-collinear spin models for the Mn surface, assuming also nonmagnetic electronic contrast for the simulation (see text).

In FIG. 7 (d) and (e) we exemplarily present two other possible models for the spin structure of the Mn surface, assuming opposite signs of the weighting factor for the nonmagnetic contribution. In FIG. 7 (e), many neighboring spins are close to parallel alignment, which is not so likely for Mn, making this spin structure less plausible than the ones shown in FIG. 7 (a) or (d). Note that, while the models presented here have a compensated spin structure in the *xy* plane, experimentally we cannot exclude a superimposed constant spin component neither along *x* nor *y*. The Mn spin structure in such a case would be compensated only when the Mn layers underneath are included. The spin arrangement of deeper Mn layers, however, is not accessible by the technique we use.

Often the Dzyaloshinskii-Moriya interaction (DMI)[36–38] is the reason for non-collinear spin structures[19–21,39,40]. However, in the low-*Z* materials considered here and, in particular, for Mn with its half-filled 3*d* shell, DMI is not expected to play a major role. We thus suggest that

- 17 -

competing and frustrated Mn–Mn antiferromagnetic exchange interactions in the reconstructed Mn film are mainly responsible for the observed non-collinear spin configuration at room temperature.

As already mentioned above, there are less long-range-ordered stripe domains with similar periodicity in 5-ML-thick areas of the Mn film compared to 6 ML Mn. A possible explanation could be segregated Co atoms within the Mn film, as discussed before. These Co atoms could act as defects on the surface and form boundaries to isolate the stripe domains or lead to an even more complicated spin configuration, which would explain why the order of the stripe-like reconstruction is more disturbed in 5-ML areas of the Mn film compared to 6 ML.
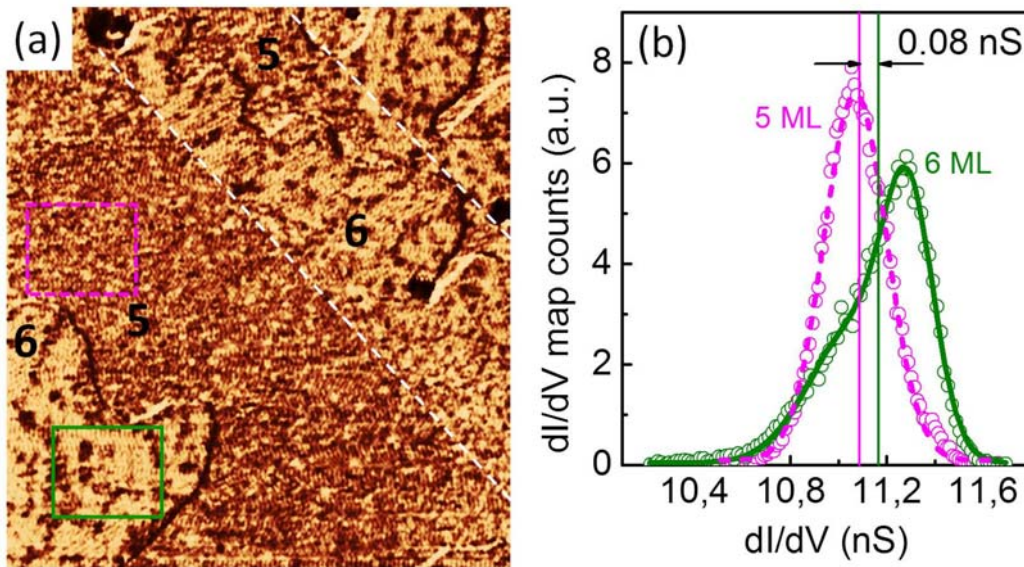

FIG. 8. (Color online) (a) Simultaneously recorded *dI/dV* map for FIG. 5 (a) at constant current mode, sample bias +0.2 V, tunneling current 2.5 nA. The dashed white line illustrates steps at the surface of the Co film underneath. (b) Histograms for the two areas at 5 and 6 ML Mn film thickness, respectively, marked by rectangles in FIG. 5 (a). Vertical solid lines show average values within the two rectangular areas, respectively.

On a larger scale, as discussed before, we have observed a weak layer-wise contrast between 5 and 6 ML Mn in FIG. 3 (b). This is also seen on the sample studied here, as shown in FIG. 8

(a), which presents a differential conductance map of the same region of the sample as shown in FIG. 5 with the same bias voltage, but different feedback parameters. Regions with 6 ML Mn appear clearly brighter than those of 5 ML. The dashed white line approximately marks step edges of the Co film underneath. On the same Mn terrace, across a Co step, the contrast changes where the Mn thickness increases from 5 to 6 ML. The two histograms in FIG. 8 (b), taken in regions of 5 and 6 ML Mn thickness as indicated by the corresponding rectangles in FIG. 8 (a), illustrate an average 0.08 nS difference, which is about only 17% of that between 4 and 5 ML Mn in FIG. 3 (d). The relative contrast is thus also about a factor 10 smaller than the atomic-scale dI/dV contrast in FIG. 5 and FIG. 6, and thus difficult to see there. While the histogram for 5 ML Mn shows a symmetric shape with a certain width, the histogram for 6 ML Mn is asymmetric with a peak at higher contrast and a tail to darker contrast. This is due to the different lengthscales of the ordered domains of reconstruction at 5 and 6 ML local Mn thicknesses. While in regions of 6 ML Mn thickness a bright contrast with dark lines in between is still recognized at the lower lateral resolution of FIG. 8 (a), the grayscale of regions of 5 ML Mn thickness is perceived as the average of very small bright and dark areas.

The simulations shown in FIG. 7 for the Mn surface spin structure would be compatible with a fully compensated spin configuration. The layer-wise large-scale contrast has proven to be quite reproducible. For its explanation no uncompensated spin structure is necessary. A likely cause is an electronic effect due to a different degree of Co segregation. The contrast between successive-ML thicknesses of Mn would then decrease with increasing thickness, as is observed in the experiment. However, as discussed before, we cannot exclude a certain superimposed layer-wise uncompensated spin component in the *xy* plane aligned by the magnetization direction of the Co layer.

Conclusion

To sum up, we have investigated the STS contrast of the e-fct Mn surface on Co/Cu(001) on

different lengthscales by Sp-STM. We found that the *dI/dV* signal is different for each thickness of the Mn layer up to 6 ML. This thickness-dependent large-scale spectroscopy contrast between successive Mn-layer thicknesses becomes weaker for increasing Mn thickness and proves to be mainly of electronic origin. Co segregation is suggested as the origin of the layer-dependent electronic properties. However, an uncompensated layered AFM spin component cannot be ruled out. On the atomic scale, there exists a geometric superstructure with a (12×2) periodicity in two types of mutually orthogonal domains on the Mn surface. The simultaneously observed differential conductance maps reveal a non-collinearity of the Mn surface spin structure at room temperature. Simple models of non-collinear Mn surface spin structures can simulate the experimental data and present possible spin configurations of the atomic-scale AFM spin structure. Co segregation may also influence the size of the reconstructed domains. The non-collinear spin structure of Mn is attributed to competing AFM exchange interactions in the frustrated and reconstructed Mn layer. We interpret the large-scale layer-wise contrast to be independent of the contrast from the atomic-scale non-collinear spin structure. These two types of spectroscopy contrast on different scales are related to the lateral resolution of the image and tip-sample distances.

References

[1] S. Heinze, M. Bode, A. Kubetzka, O. Pietzsch, X. Nie, S. Blügel, and R. Wiesendanger, Science **288**, 1805 (2000).

[2] D. Spišák and J. Hafner, Phys. Rev. B **61**, 12728 (2000).

[3] M. Bode, E.Y. Vedmedenko, K. von Bergmann, A. Kubetzka, P. Ferriani, S. Heinze, and R.

Wiesendanger, Nat. Mater. **5**, 477 (2006).

[4] W. Kuch, L.I. Chelaru, F. Offi, J. Wang, M. Kotsugi, and J. Kirschner, Nat. Mater. **5**, 128 (2006).

[5] K. Lenz, S. Zander, and W. Kuch, Phys. Rev. Lett. **98**, 237201 (2007).

[6] S. Loth, S. Baumann, C.P. Lutz, D.M. Eigler, and A.J. Heinrich, Science **335**, 196 (2012).

[7] M.Y. Khan, C.-B. Wu, M. Erkovan, and W. Kuch, J. Appl. Phys. **113**, 023913 (2013).

[8] W.H. Meiklejohn and C.P. Bean, Phys. Rev. **105**, 904 (1957).

[9] J. Hafner and D. Hobbs, Phys. Rev. B **68**, 014408 (2003).

[10] M. Zelený, F.D. Natterer, A. Biedermann, and J. Hafner, Phys. Rev. B **82**, 165422 (2010).

[11] R.G.P. van der Kraan and H. van Kempen, Surf. Sci. **338**, 19 (1995).

[12] M. Wuttig, C.C. Knight, T. Flores, and Y. Gauthier, Surf. Sci. **292**, 189 (1993).

[13] Y.S. Dedkov, E.N. Voloshina, and M. Fonin, Surf. Sci. **600**, 4328 (2006).

[14] C.L. Gao, U. Schlickum, W. Wulfhekel, and J. Kirschner, Phys. Rev. Lett. **98**, 107203 (2007).

[15] J.T. Kohlhepp and W.J.M. de Jonge, Phys. Rev. Lett. **96**, 237201 (2006).

[16] J. Hafner and D. Spišák, Phys. Rev. B **72**, 144420 (2005).

[17] R. Wiesendanger, I.V. Shvets, D. Bürgler, G. Tarrach, H.J. Güntherodt, J.M.D. Coey, and S. Gräser, Science **255**, 583 (1992).

[18] R. Wiesendanger, Rev. Mod. Phys. **81**, 1495 (2009).

[19] M. Bode, M. Heide, K. von Bergmann, P. Ferriani, S. Heinze, G. Bihlmayer, A. Kubetzka, O. Pietzsch, S. Blügel, and R. Wiesendanger, Nature **447**, 190 (2007).

[20] P. Ferriani, K. von Bergmann, E.Y. Vedmedenko, S. Heinze, M. Bode, M. Heide, G. Bihlmayer, S. Blügel, and R. Wiesendanger, Phys. Rev. Lett. **101**, 027201 (2008).

[21] Y. Yoshida, S. Schröder, P. Ferriani, D. Serrate, A. Kubetzka, K. von Bergmann, S. Heinze, and R. Wiesendanger, Phys. Rev. Lett. **108**, 087205 (2012).

[22] P.-J. Hsu, C.-I. Lu, Y.-H. Chu, B.-Y. Wang, C.-B. Wu, L.-J. Chen, S.-S. Wong, and M.-T. Lin, Phys. Rev. B **85**, 174434 (2012).

[23] C.-B. Wu, J. Song, and W. Kuch, Appl. Phys. Lett. **101**, 012404 (2012).

[24] A.K. Schmid and J. Kirschner, Ultramicroscopy **42–44, Part 1**, 483 (1992).

[25] J.R. Cerda, P.L. de Andres, A. Cebollada, R. Miranda, E. Navas, P. Schuster, C.M. Schneider, and J. Kirschner, J. Phys. Condens. Matter **5**, 2055 (1993).

[26] J.T. Kohlhepp, H. Wieldraaijer, and W.J.M. de Jonge, Appl. Phys. Lett. **89**, 032507 (2006).

[27] J.T. Kohlhepp, H. Wieldraaijer, and W.J.M. de Jonge, J. Mater. Res. **22**, 569 (2007).

[28] B. Zhang, C.-B. Wu, and W. Kuch, J. Appl. Phys. **115**, 233915 (2014).

[29] W.L. O'Brien and B.P. Tonner, Phys. Rev. B **50**, 2963 (1994).

[30] A. Noguera, S. Bouarab, A. Mokrani, C. Demangeat, and H. Dreyssé, J. Magn. Magn. Mater. **156**, 21 (1996).

[31] C.-B. Wu, Master thesis, National Taiwan University, Taipei (2004).

[32] M. Wuttig, Y. Gauthier, and S. Blügel, Phys. Rev. Lett. **70**, 3619 (1993).

[33] A. Dittschar, W. Kuch, M. Zharnikov, and C.M. Schneider, J. Magn. Magn. Mater. **212**, 307 (2000).

[34] S. Müller, P. Bayer, C. Reischl, K. Heinz, B. Feldmann, H. Zillgen, and M. Wuttig, Phys. Rev. Lett. **74**, 765 (1995).

[35] R. Wiesendanger, H.-J. Güntherodt, G. Güntherodt, R.J. Gambino, and R. Ruf, Phys. Rev. Lett. **65**, 247 (1990).

[36] I. Dzialoshinskii, Sov. Phys. JETP **5,** 1259 (1957).

[37] I. Dzyaloshinsky, J. Phys. Chem. Solids **4**, 241 (1958).

[38] T. Moriya, Phys. Rev. **120**, 91 (1960).

[39] K. von Bergmann, A. Kubetzka, O. Pietzsch, and R. Wiesendanger, J. Phys. Condens. Matter **26**, 394002 (2014).

[40] K. von Bergmann, M. Menzel, D. Serrate, Y. Yoshida, S. Schröder, P. Ferriani, A. Kubetzka, R. Wiesendanger, and S. Heinze, Phys. Rev. B **86**, 134422 (2012).